

Nonvolatile Magnonics in Bilayer Magnetic Insulators

Jinyang Ni,^{*,†,‡,¶} Zhenlong Zhang,^{†,¶} Jinlian Lu,[§] Quanchao Du,[‡] Zhijun Jiang,^{*,†,||}
and Laurent Bellaiche^{⊥,#}

[†]*Ministry of Education Key Laboratory for Nonequilibrium Synthesis and Modulation of Condensed Matter, Shaanxi Province Key Laboratory of Advanced Functional Materials and Mesoscopic Physics, School of Physics, Xi'an Jiaotong University, Xi'an 710049, China*

[‡]*Division of Physics and Applied Physics, School of Physics and Mathematical Sciences, Nanyang Technological University, Singapore 637731, Singapore*

[¶]*These authors contributed equally to this work.*

[§]*Department of Physics, Yancheng Institute of Technology, Yancheng, Jiangsu 224051, China*

^{||}*Key Laboratory of Computational Physical Sciences (Ministry of Education), Institute of Computational Physical Sciences, State Key Laboratory of Surface Physics and Department of Physics, Fudan University, Shanghai 200433, China*

[⊥]*Smart Ferroic Materials Center, Physics Department and Institute for Nanoscience and Engineering, University of Arkansas, Fayetteville, Arkansas 72701, USA*

[#]*Department of Materials Science and Engineering, Tel Aviv University, Ramat Aviv, Tel Aviv 6997801, Israel*

E-mail: jinyang.ni@ntu.edu.sg; zjjiang@xjtu.edu.cn

Abstract

Nonvolatile control of spin order or spin excitations offers a promising avenue for advancing spintronics; however, practical implementation remains challenging. In this letter, we propose a general framework to realize electrical control of magnons in 2D magnetic insulators. We demonstrate that in bilayer ferromagnetic insulators with strong spin-layer coupling, electric field E_z can effectively manipulate the spin exchange interactions between the layers, enabling nonvolatile control of the corresponding magnons. Notably, in this bilayer, E_z can induce nonzero Berry curvature and orbital moments of magnons, the chirality of which are coupled to the direction of E_z . This coupling facilitates E_z manipulate the corresponding magnon valley and orbital Hall currents. Furthermore, such bilayers can be easily engineered, as demonstrated by our density-functional-theory calculations on Janus bilayer Cr-based ferromagnets. Our work provides an important step toward realizing nonvolatile magnonics and paves a promising way for future magnetoelectric coupling devices.

Keywords: Nonvolatile control, Magnons, Berry curvature, Orbital moments, Magnon Hall current

Introduction. In ordered magnets, spins tend to align in a regular pattern due to strong exchange interactions¹⁻³. When one or more spins are perturbed, this disturbance can propagate through the material as a wave, representing a collective excitation of the spins. The quanta of spin waves, known as magnons^{4,5}, play a fundamental role in understanding magnetic properties^{6,7}. Analogous to electric currents, magnon-based currents can be used to carry, transport and process information^{4,8-20}. In particular, magnons can possess nanometer-scale wavelengths^{21,22}, operate in the terahertz (THz) frequency range^{23,24}, and enable the transfer of spin information over macroscopic distances^{21,25}. These characteristics pave new avenues for wave-based computing technologies that are Joule-heat-free, addressing the fundamental limitations of modern electronics.

In practical implementations, nonvolatile manipulation of magnons, particularly through electric fields, remains a significant challenge for various reasons^{21,26,27}. One of the key challenge is to establish an efficient coupling between magnons and electric field^{28,29}. For instance, to control the magnon density, a substantial electric field induced modification of spin-wave dispersions is generally required^{30,31}. A possible route toward this goal involves the use of magnetoelectric materials capable of modulating spin exchange interactions via the electric field. However, such materials have yet to be synthesized experimentally³²⁻³⁷. Furthermore, the magnon quantity carrying spin information, such as spin or orbital angular momentum, are typically decoupled from the electric field³⁸⁻⁴⁰. Therefore, developing a comprehensive strategy for an effective electric field control of magnons is highly desired.

In this work, we present a general framework to realize electrical control of magnons in 2D magnetic insulators. We demonstrate that in bilayer ferromagnetic insulators, where each layer breaks the inversion symmetry and two layers connected by the mirror symmetry \mathcal{M}_z , strong spin-layer coupling can emerge. This spin-layer coupling enables the out-of-plane electric field E_z to manipulate the spin exchange interactions between the layers, realizing a nonvolatile control of its magnons. By performing spin model analysis and density-functional-theory (DFT) calculations, we identify that Cr-based Janus bilayers exhibit strong spin-layer coupling with respect to E_z . Since E_z breaks the inversion symmetry, it can induce and manipulate the magnon Berry curvature as well as the magnon orbital moments. Additionally, E_z can also generate orbital Berry curvature of magnons, which contribute to a

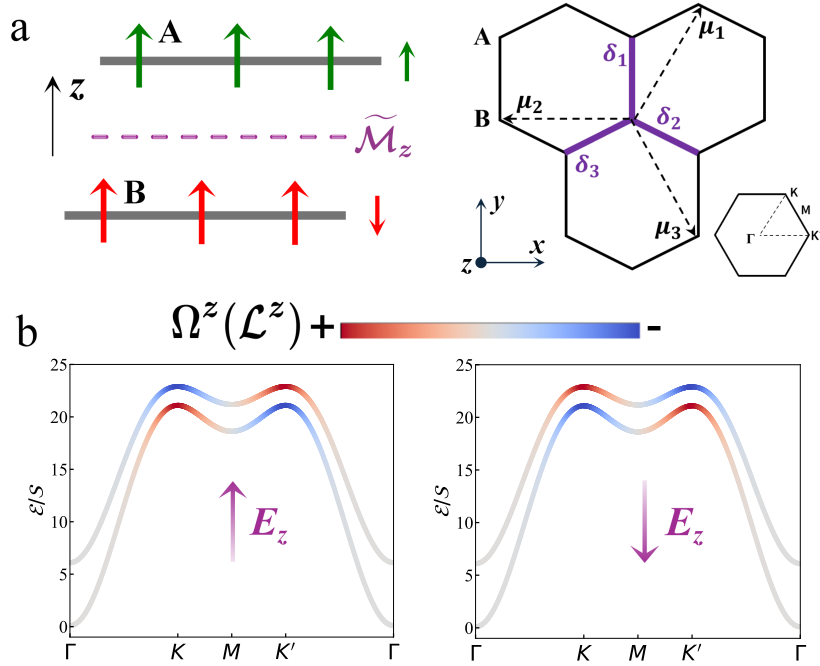


Figure 1: (a)Left: side view of the of AB-stacked bilayer triangular ferromagnet, where the polar vectors in top and bottom layers are opposite oriented. The $\widetilde{\mathcal{M}}_z$ combines both horizontal mirror symmetry and translation symmetry. Right: top view of such a bilayer ferromagnet. (b) The illustration of electric field control of the orbital moments and Berry curvature of magnons.

significant magnon orbital Hall current. This mechanism enables ultrafast control of magnon Hall transport via an electric field.

General theory. We firstly consider the AB-stacked bilayer magnet, which consist of two triangular ferromagnets layers coupled through ferromagnetic interactions. As schematically illustrated in Figure 1a, this bilayer triangular ferromagnet is analogous to a monolayer honeycomb ferromagnet. In this analogy, the nearest-neighbor (NN) intralayer spin exchange within the upper or bottom layer corresponds to the next-nearest-neighbor (2NN) spin exchange along the A-A or B-B paths in the honeycomb lattice. Similarly, the NN interlayer spin exchange corresponds to the NN intralayer spin exchange interaction of a monolayer honeycomb lattice. Compared with the conventional bilayer ferromagnets, our bilayer model exhibits two key distinctions in symmetry: (i) the inversion symmetry \mathcal{P} within each layer is broken, and (ii) the effective horizontal mirror reflection $\widetilde{\mathcal{M}}_z$ or inversion symmetry \mathcal{P} of this bilayer is preserved. Protected by these symmetry operations, the polar vectors of the top and bottom layers are oppositely oriented, as shown in Figure 1a. This feature gives rise to a robust magnetoelectric effect⁴¹, where the E_z not only induces the net polarization but also modifies the spin polarization of this bilayer. Correspondingly, the spin associated quantity of wave functions within each layer can be tuned by E_z , thus enabling spin-layer coupling. This coupling, in turn, allows the spin exchange interactions to be controlled via the E_z .

Following the above symmetry requirement, the minimum spin model of this bilayer ferromagnet can write as

$$\hat{\mathcal{H}} = \mathcal{J}_{ab} \sum_{\langle i,j \rangle} \mathcal{S}_i \cdot \mathcal{S}_j + \mathcal{J}_a \sum_{\langle i,j \rangle} \mathcal{S}_i \cdot \mathcal{S}_j + \mathcal{J}_b \sum_{\langle i,j \rangle} \mathcal{S}_i \cdot \mathcal{S}_j + \mathcal{K}_a \sum_i \mathcal{S}_{i,z}^2 + \mathcal{K}_b \sum_i \mathcal{S}_{i,z}^2, \quad (1)$$

where \mathcal{J}_{ab} represents NN interlayer spin exchange interaction, $\mathcal{J}_{a(b)}$ denotes NN intralayer spin exchange interactions in the top (bottom) layer, and $\mathcal{K}_{a(b)}$ refers to the easy-axis single-ion-anisotropy (SIA) at top(bottom) layer. The linear spin wave model in Eq. (1) can be solved by employing Holstein-Primakoff (HP) transformation⁴², $\mathcal{S}_{i,\alpha}^z = S - \hat{a}_{i,\alpha}^\dagger \hat{a}_{i,\alpha}$, $\mathcal{S}_i^+ \approx \sqrt{2S} \hat{a}_{i,\alpha}$ and $\mathcal{S}_{i,\alpha}^- \approx \sqrt{2S} \hat{a}_{i,\alpha}^\dagger$ where $\hat{a}_{i,\alpha}^\dagger$ creates a magnon on α sublattice (A, B) in the i -th unit cell. Upon Fourier transformation, the Hamiltonian can be expressed in the basis

$\psi_k^\dagger \equiv (\hat{a}_k^\dagger, \hat{b}_k^\dagger)$ as $\hat{\mathcal{H}} = \sum_k \psi_k^\dagger \hat{\mathcal{H}}_k \psi_k$. Neglecting the zero-point energy, $\hat{\mathcal{H}}_k$ reads as,

$$\hat{\mathcal{H}}_k/S = -3\mathcal{J}_{ab} + \begin{pmatrix} \mathcal{J}_a f_k - 2\mathcal{K}_a & \mathcal{J}_{ab} \gamma_k \\ \mathcal{J}_{ab} \gamma_k^\dagger & \mathcal{J}_b f_k - 2\mathcal{K}_b \end{pmatrix}, \quad (2)$$

where $\gamma_k = \sum_{\delta} e^{-i\mathbf{k} \cdot \delta_i}$ and $f_k = \sum_{i \in \text{odd}} 2\cos(\mathbf{k} \cdot \boldsymbol{\mu}_i) - 6$ with $\boldsymbol{\delta}_i$ and $\boldsymbol{\mu}_i$ being NN and 2NN linking vectors of honeycomb lattice as shown in Figure 1a.

For simplicity, Eq. (2) can be parameterized as $h_0 = \frac{1}{2}(\mathcal{J}_a + \mathcal{J}_b)f_k - (\mathcal{K}_a + \mathcal{K}_b)$, $h_x = \mathcal{J}_{ab}\text{Re}\gamma_k$, $h_y = \mathcal{J}_{ab}\text{Im}\gamma_k$ and $h_z = \frac{1}{2}(\mathcal{J}_a - \mathcal{J}_b)f_k - (\mathcal{K}_a - \mathcal{K}_b)$. Eq. (2) can thus be expressed in terms of Pauli-matrices $\boldsymbol{\sigma} = (\sigma_x, \sigma_y, \sigma_z)$, given as

$$\hat{\mathcal{H}}_k/S = h_0 I + \mathbf{h}(\mathbf{k}) \cdot \boldsymbol{\sigma}, \quad (3)$$

where $\mathbf{h}(\mathbf{k}) = (h_x, h_y, h_z) = |h|(\sin\theta\cos\phi, \sin\theta\sin\phi, \cos\theta)$. The corresponding eigenvalues and eigenvectors are given by

$$\epsilon_{\pm}/S = h_0 \pm |\mathbf{h}(\mathbf{k})|, \quad \Psi_{\pm} = \begin{pmatrix} \sqrt{1 \pm \cos\theta} \\ \pm e^{-i\phi} \sqrt{1 \mp \cos\theta} \end{pmatrix}. \quad (4)$$

Clearly, the emergence of h_z breaks the sublattice symmetry of honeycomb lattice and open a gap of magnon bands at K-points. Under this condition, the time reversal symmetry (\mathcal{T}) is preserved and the inversion symmetry \mathcal{P} is broken¹⁵, resulting in a nonzero Berry curvature. In 2D cases, the Berry curvature only have z -component, which can be expressed in term of the $\mathbf{h}(\mathbf{k})$ vectors,

$$\Omega_{\pm}^z(\mathbf{k}) = -i\langle \nabla \Psi_{\pm} | \times | \nabla \Psi_{\pm} \rangle = \mp \frac{h_z}{2} (\nabla h_x \times \nabla h_y). \quad (5)$$

Consequently, in this bilayer, the nonzero Berry curvature depend on the values of $\mathcal{J}_a - \mathcal{J}_b$ and $\mathcal{K}_a - \mathcal{K}_b$, indicating the chirality of magnon Berry curvature can be controlled by E_z . Notably, the magnon Berry curvature is absent in the monolayer due to the presence of only

a single magnon branch.

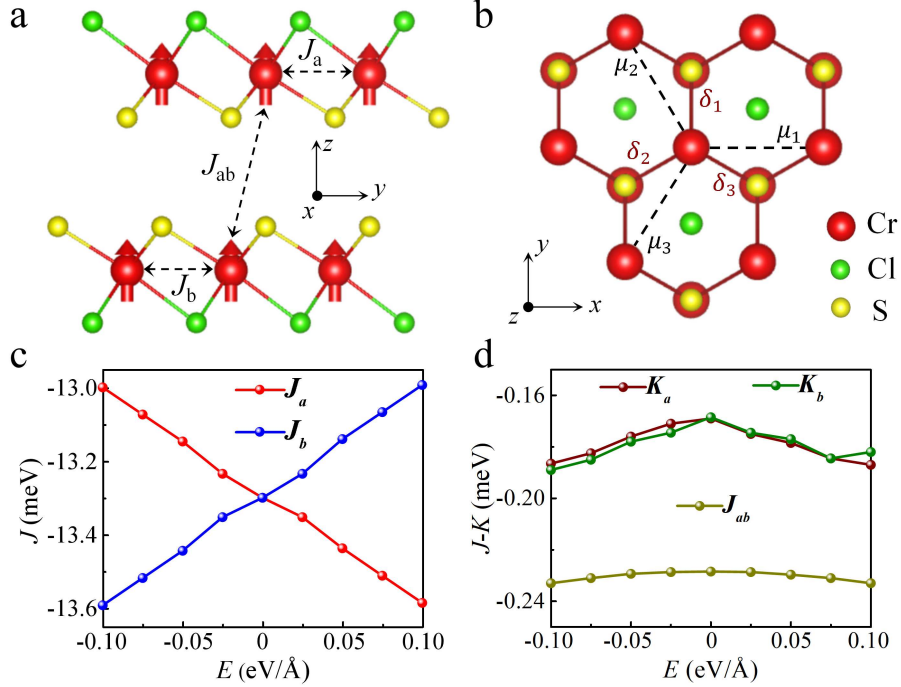


Figure 2: (a) Side view of the geometrical structure of AB-stacked bilayer CrSCl. (b) Top view of the bilayer CrSCl. (c)-(d) The dependence of intralayer spin exchange interactions $\mathcal{J}_a(\mathcal{J}_b)$, interlayer spin exchange interaction \mathcal{J}_{ab} and SIA $\mathcal{K}_a(\mathcal{K}_b)$ on E_z in bilayer CrSCl.

In addition to the Berry curvature, the nonzero h_z can also induce orbital moments of magnons^{38–40}. To study this orbital quantity, we invoke the semiclassical formulation of the wave packet dynamics of Bloch magnons^{43,44}, which is given by

$$\mathcal{L}_{m,\pm}^z(\mathbf{k}) = -\frac{i}{2\hbar} \langle \nabla \Psi_{\pm} | \times (\hat{\mathcal{H}}_k - \bar{\epsilon}_k) | \nabla \Psi_{\pm} \rangle. \quad (6)$$

Compared to the Berry curvature of magnons, the orbital moments also depend on the h_z ; however, the chirality of orbital moments is identical for the majority and minority bands. Note that the orbital angular momentum (\mathcal{L}^z) and orbital moments (\mathcal{L}_m^z) of magnons differ only by a factor related to mass term. Therefore, Berry curvature and orbital moments of magnons can be induced and manipulated by electric field in the bilayer ferromagnetic insulators with strong spin-layer coupling.

Layer spin coupling in bilayer CrXY. Having established the concept of electrically

switchable magnons in bilayer ferromagnets based on the effective model, we next illustrate this with a concrete example of Janus bilayer 1T-CrXY ($X = \text{S, Se}; Y = \text{Cl, Br}$). Janus monolayer 1T-CrXY is derived from the well-known monolayer Cr-based dichalcogenide 1T-CrTe₂, where the chalcogen layer substituted by halides, leading to in a transition from the metallic to insulator states⁴⁵⁻⁴⁹. In monolayer CrXY, the Cr³⁺ ions with $S = 3/2$ form a triangular lattice, where the inversion symmetry \mathcal{P} is broken. Building upon this monolayer, bilayer CrXY adopts an AB-stacking configuration with Y - X - X - Y order, preserving the \mathcal{P} , as illustrated in Figure 2a. The structure stability of bilayer Janus 1T-CrXY is confirmed through the phonon dispersion calculation and molecular dynamics simulation, with details shown in Supporting Information (SI⁵⁰). By employing energy mapping method^{51,52}, we calculate the interlayer and intralayer spin exchange interactions of bilayer CrXY, both of which are ferromagnetic, as shown in Table 1, confirming its the ferromagnetic ground state. It is noteworthy that the magnetic anisotropy of bilayer CrSY and CrSeY differs; the former exhibits easy-axis, while the latter shows easy plane, as indicated by the sign of \mathcal{K} . As shown in Figure S7⁵⁰, the calculated orbital-resolved magnetic anisotropy energy (MAE) reveals that the MAE of CrXY mainly depends on the hybridizations of $3d$ -orbitals of Cr³⁺ between p -orbitals of X^{2-} and Y^- . For CrSY, the dominant contributions to the easy-axis MAE originate from Cr³⁺ and Y^- ions, resulting in easy-axis magnetic anisotropy. In contrast, significant easy-plane contributions from Se²⁻ drive the easy-plane magnetic anisotropy of CrSeY. Unless otherwise specified, the following discussion primarily focuses on the bilayer CrSCl for simplicity.

Table 1: Calculated spin exchange parameters (with units of meV) of Janus bilayer CrXY without E_z .

<i>Mat.</i>	\mathcal{J}_{ab}	\mathcal{J}_a (\mathcal{J}_b)	\mathcal{K}_a (\mathcal{K}_b)
CrSCl	-0.23	-13.31	-0.17
CrSBr	-0.21	-14.48	-0.23
CrSeCl	-0.24	-11.77	0.21
CrSeBr	-0.11	-14.49	0.11

When $E_z = 0$, the \mathcal{P} ensures that the localized spin moments of Cr³⁺ ions within each layer of bilayer CrSCl are identical. Consequently, the NN intralayer spin exchange

interactions and SIA between the top and bottom layers are identical, i.e., $\mathcal{J}_a = \mathcal{J}_b$ and $\mathcal{K}_a = \mathcal{K}_b$. Upon applying E_z , \mathcal{P} is naturally broken, disrupting this balance. Specially, for $E_z = 0.1 \text{ eV}/\text{\AA}$, the difference in localized spin moments of Cr^{3+} ions between two layers reaches approximately $0.005 \mu_B$. This imbalance is notably reflected in the remarkable changes to the spin exchange parameters between the two layers, as illustrated in Figure 2c, where $\mathcal{J}_b - \mathcal{J}_a = 0.6 \text{ meV}$ with $E_z = 0.1 \text{ eV}/\text{\AA}$. As the strength of E_z increases, $\mathcal{J}_a - \mathcal{J}_b$ exhibits a linear dependence on E_z , described by $\mathcal{J}_a - \mathcal{J}_b = -6E_z$, indicating that electric field can reverse the sign of $\mathcal{J}_a - \mathcal{J}_b$. In contrast to the Heisenberg exchange interactions, the change in $\mathcal{K}_a - \mathcal{K}_b$ with respect to E_z is slower due to the weak SOC of bilayer CrSCL, so we can assume $\mathcal{K}_a = \mathcal{K}_b$ in the following discussion. Similarly, the Dzyaloshinskii-Moriya interaction of bilayer CrSCL is relatively weak⁴⁸, and its response to E_z is negligible. In addition, the NN intralayer coupling, \mathcal{J}_{ab} , can be enhanced by E_z , reaching -0.25 meV when $E_z = 0.2 \text{ eV}/\text{\AA}$. According to Eqs. (5)-(6), a significant $\mathcal{J}_a - \mathcal{J}_b$ can give rise to the nonzero Berry curvature and orbital moments of magnons, with their chirality being coupled to the E_z .

Nonvolatile control of magnon transport. In Figure 3a, we observe that the Berry curvature of magnons at $E_z = 0.05 \text{ eV}/\text{\AA}$ is primarily concentrated at the K-points and satisfy $\boldsymbol{\Omega}(\mathbf{k}) = -\boldsymbol{\Omega}(-\mathbf{k})$, indicating the inversion symmetry \mathcal{P} of magnons is broken. In this case, the net magnon Hall current, the first order thermal Hall response under the temperature gradient, remains zero due to the opposite contributions of magnon Berry curvature at K and K'-points. However, the opposite orbit pseudo-magnetic field at K and K'-points give rise to the magnon valley current, similar to the gapped graphene^{53,54}. To distinguish the difference between K and K'-points⁵⁵, we define the magnon valley conductivity κ_{xy}^v as

$$\kappa_{xy}^v = \frac{k_B^2 T}{\hbar V} \sum_{n,k} c_2(\rho) [\Omega_{n,k}(\text{K}) - \Omega_{n,k}(\text{K}')], \quad (7)$$

where V is the volume, ε_{abc} is the Levi-Civita symbol with $abc = xyz$ and $c_2(\rho) = \int_0^\rho [\log(1 + \rho^{-1})]^2 d\rho$ with ρ being Boltzmann distributions for bosons. Figure 4a illustrates the nonlinear dependence of κ_{xy}^v on E_z at a fixed temperature. Specifically, κ_{xy}^v starts from zero, reaches maximum at $E_z = 0.05 \text{ eV}/\text{\AA}$ ($\mathcal{J}_a - \mathcal{J}_b = -0.3 \text{ meV}$), then decreases. Since the E_z can

reverse the sign of $\mathcal{J}_a - \mathcal{J}_b$, the chirality of Berry curvature at K-points and the sign of κ_{xy}^v can be electrically controlled.

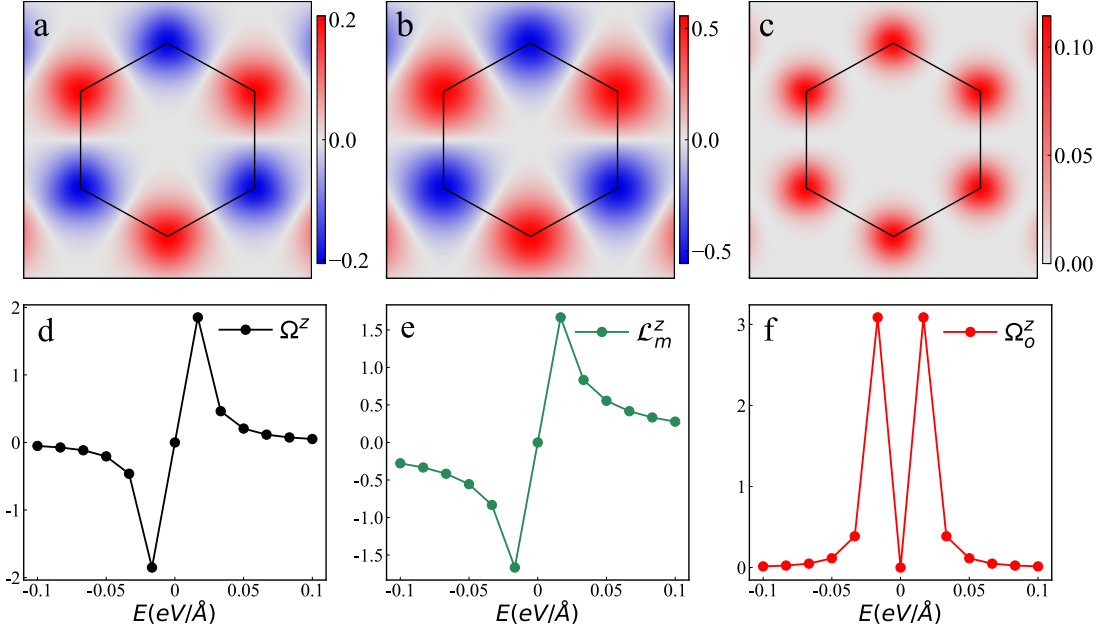


Figure 3: (a)-(c) Berry curvature (Ω^z), orbital moments (\mathcal{L}_m^z), and orbital Berry curvature (Ω_o^z) of minor magnon band in bilayer CrSCl with $E_z = 0.05$ eV/Å. (d)-(f) The dependence of Ω^z , \mathcal{L}_m^z , and Ω_o^z at K-points on E_z .

As shown in Eq. (6), in addition to the Berry curvature, the nonzero $h_z \approx (\mathcal{J}_a - \mathcal{J}_b)f_k$ can induce the magnon orbital moments, indicating that E_z can effectively manipulate the magnon orbital quantity. Figure 3b illustrates the orbital moments of magnons at $E_z = 0.05$ eV/Å, indicating that orbital moments primarily reside at K-points and exhibit opposite signs at different K-points, similar to behavior of the Berry curvature. Because $\mathcal{J}_a - \mathcal{J}_b$ is governed by E_z , the orbital moments or orbital angular momentum of magnons can be switched electrically, as evidenced in Figure 3e.

The emergence of magnon orbital moments gives rise to the anomalous orbital associated transport phenomena^{40,54}. As shown in the SI⁵⁰, we derived the analytical expression for magnons orbital Berry curvature, Ω_o^z , defined as follows

$$\Omega_o^z(\mathbf{k}) = \Omega^z(\mathbf{k})\mathcal{L}_m^z(\mathbf{k}). \quad (8)$$

Obviously, the orbital Berry curvature is the product of the Berry curvature and the orbital

moments of magnons^{40,54}. As both the Berry curvature and orbital moments are odd with respect to \mathbf{k} , their product, orbital Berry curvature, is even, $\mathbf{\Omega}_o^z(\mathbf{k}) = \mathbf{\Omega}_o^z(-\mathbf{k})$, breaking the effective time-reversal symmetry in orbital space. This characteristic enables the emergence of the net magnon Hall current, in contrast to the contribution from the Berry curvature alone, as shown in Figure 4. Thus, analogous to the magnon Hall effect, the magnon orbital Hall conductivity is determined by integrating the product of $c_2(p)$ and $\mathbf{\Omega}_o^z$ over the first Brillouin zone, expressed as follows

$$\kappa_{xy}^o = \frac{k_B^2 T}{\hbar V} \sum_{n,k} c_2(\rho) \Omega_{n,o}^z(k). \quad (9)$$

Figure 4b shows that the dependence of κ_{xy}^o on E_z is even, which can be attributed to the even relationship between the orbital Berry curvature and E_z . Notably, κ_{xy}^o decreases with increasing E_z and diverges as E_z approaches zero. This divergence arises because the Berry curvature and orbital moments of each band vanish across most of the momentum space, except at the K-points, when E_z is small. As a result, the orbital Berry curvature diverges as E_z approaches zero as well as the the orbital Hall conductivity.

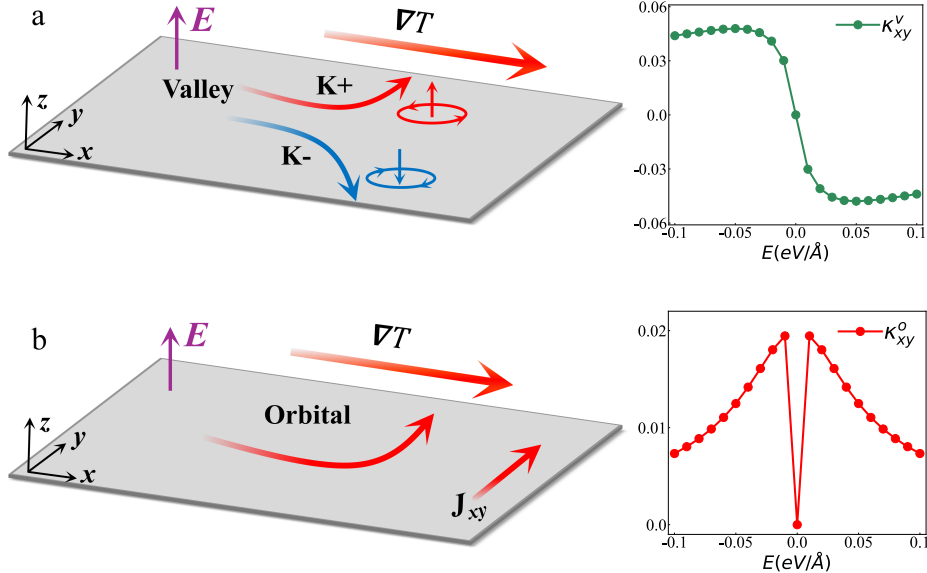


Figure 4: (a) The left panel illustrates the magnon valley Hall effect. The right panel shows the dependence of the magnon valley conductivity κ_{xy}^v on E_z . (b) The left panel illustrates the magnon orbital Hall effect. The right panel shows the dependence of the orbital Hall conductivity κ_{xy}^o on the E_z . Both κ_{xy}^v and κ_{xy}^o are expressed in units of k_B^2/\hbar .

Bilayer honeycomb ferromagnets. The picture of electrical control of magnons can also be applied to Janus bilayer honeycomb ferromagnets, such as $\text{Cr}_2\text{Br}_3\text{Cl}_3$ ^{56,57}. The ground state of Janus bilayer $\text{Cr}_2\text{Br}_3\text{Cl}_3$ adopts AB-stacked configuration, where the intralayer and interlayer coupling are both ferromagnetic, as confirmed by our DFT calculations presented in SI⁵⁰. When $E_z = 0$, the \mathcal{PT} symmetry of its magnons is preserved, and the corresponding magnon bands exhibits three-fold degeneracy at K-points. When E_z is applied, the local spin moments of Cr^{3+} ions will differ between layers, similar to the Janus bilayer CrXY . This spin-layer coupling modifies the spin exchange interactions and SIA within each layer, breaking the inversion symmetry \mathcal{P} of magnons. Consequently, this can lift the threefold degeneracy in the magnon bands at K-points, generating nonzero Berry curvature and orbital moments, which in turn induce magnon valley and orbital Hall currents. Compared with bilayer CrXY , the sublattice symmetry of honeycomb lattice within each layer in bilayer $\text{Cr}_2\text{Br}_3\text{Cl}_3$ remains preserved even when $E_z \neq 0$. Consequently, the Berry curvature and orbital moments of corresponding magnon bands are even with respect to the E_z .

In addition to the Janus bilayer, bilayer 2H-type magnets, such as bilayer 2H- $M\text{Se}_2$ with ($M = \text{V}, \text{Cr}, \text{Mn}$), also satisfy the symmetry requirement outlined above^{45,58-64}. The numerous candidate materials provide strong evidence for the applicability of our theory and offer a broader range of options for experimental realization.

Summary and discussion. In summary, we propose a general framework for achieving electrical control of magnons in bilayer ferromagnetic insulators with strong spin-layer coupling. We demonstrate that the strong spin-layer coupling allows the electric field to manipulate the spin exchange interactions between layers, as evidenced by our DFT calculations on Janus bilayer Cr-based ferromagnetic insulators. This capability facilitates the electrical control of strength and chirality of magnons, encompassing their Berry curvature, orbital moments, and orbital Berry curvature. Therefore, the magnon valley Hall and orbital Hall transport can be effectively tuned by applying an electric field. The broad applicability of our findings, coupled with the diverse array of material candidates identified, lays a solid foundation for the development of high-speed, compact spintronic and magnonic devices.

ASSOCIATED CONTENT

Supporting Information

In this Supporting Information, we provide: I. the details of DFT calculations and additional calculations of Janus bilayers CrSCl and Cr₂Br₃Cl₃; II. the magnetic anisotropy of bilayer CrXY. III. the details of the orbital Berry curvature of magnons; and IV. the magnon Hamiltonian of bilayer Cr₂Br₃Cl₃.

AUTHOR INFORMATION

Jinyang Ni and Zhenlong Zhang equally contributed to this work.

Corresponding Authors

*E-mail: jinyang.ni@ntu.edu.sg (J. N.)

*E-mail: zjjiang@xjtu.edu.cn (Z. J.)

Notes

The authors declare no competing financial interest.

ACKNOWLEDGMENTS

The authors thank Prof. Yuanjun Jin for helpful discussions. This work is supported by the National Natural Science Foundation of China (Grant No. 12374092), Natural Science Basic Research Program of Shaanxi (Program No. 2023-JC-YB-017), Shaanxi Fundamental Science Research Project for Mathematics and Physics (Grant No. 22JSQ013), “Young Talent Support Plan” of Xi’an Jiaotong University (Grant No. WL6J004), the Open Project of State Key Laboratory of Surface Physics (Grant No. KF2023_06), and the Xiaomi Young Talents Program. L. B. thanks the Vannevar Bush Faculty Fellowship Grant No. N00014-20-1C2834 from the Department of Defense and Grant No. DMR-1906383 from the National Science Foundation Q-AMASE-i Program (MonArk NSF Quantum Foundry).

References

- (1) Néel, L. Propriétés magnétiques des ferrites; ferrimagnétisme et antiferromagnétisme. *Ann. Phys.* **1948**, *12*, 137–198.
- (2) Keffer, F.; Kittel, C. Theory of antiferromagnetic resonance. *Phys. Rev.* **1952**, *85*, 329.
- (3) Anderson, P. W. Antiferromagnetism. Theory of superexchange interaction. *Phys. Rev.* **1950**, *79*, 350.
- (4) Chumak, A. V.; Vasyuchka, V. I.; Serga, A. A.; Hillebrands, B. Magnon spintronics. *Nat. Phys.* **2015**, *11*, 453–461.
- (5) Lenk, B.; Ulrichs, H.; Garbs, F.; Münzenberg, M. The building blocks of magnonics. *Phys. Rep.* **2011**, *507*, 107–136.
- (6) Prabhakar, A.; Stancil, D. D. *Spin waves: Theory and applications*; Springer, 2009; Vol. 5.
- (7) Pirro, P.; Vasyuchka, V. I.; Serga, A. A.; Hillebrands, B. Advances in coherent magnonics. *Nat. Rev. Mater.* **2021**, *6*, 1114–1135.
- (8) Onose, Y.; Ideue, T.; Katsura, H.; Shiomi, Y.; Nagaosa, N.; Tokura, Y. Observation of the magnon Hall effect. *Science* **2010**, *329*, 297–299.
- (9) Katsura, H.; Nagaosa, N.; Lee, P. A. Theory of the thermal Hall effect in quantum magnets. *Phys. Rev. Lett.* **2010**, *104*, 066403.
- (10) Matsumoto, R.; Shindou, R.; Murakami, S. Thermal Hall effect of magnons in magnets with dipolar interaction. *Phys. Rev. B* **2014**, *89*, 054420.
- (11) Zyuzin, V. A.; Kovalev, A. A. Magnon spin Nernst effect in antiferromagnets. *Phys. Rev. Lett.* **2016**, *117*, 217203.
- (12) Cheng, R.; Okamoto, S.; Xiao, D. Spin Nernst effect of magnons in collinear antiferromagnets. *Phys. Rev. Lett.* **2016**, *117*, 217202.

- (13) Li, K.; Li, C.; Hu, J.; Li, Y.; Fang, C. Dirac and nodal line magnons in three-dimensional antiferromagnets. *Phys. Rev. Lett.* **2017**, *119*, 247202.
- (14) Bao, S.; Wang, J.; Wang, W.; Cai, Z.; Li, S.; Ma, Z.; Wang, D.; Ran, K.; Dong, Z.-Y.; Abernathy, D.; et al. Discovery of coexisting Dirac and triply degenerate magnons in a three-dimensional antiferromagnet. *Nat. Commun.* **2018**, *9*, 2591.
- (15) Mook, A.; Plekhanov, K.; Klinovaja, J.; Loss, D. Interaction-stabilized topological magnon insulator in ferromagnets. *Phys. Rev. X* **2021**, *11*, 021061.
- (16) Chen, L.; Chung, J.-H.; Gao, B.; Chen, T.; Stone, M. B.; Kolesnikov, A. I.; Huang, Q.; Dai, P. Topological spin excitations in honeycomb ferromagnet CrI₃. *Phys. Rev. X* **2018**, *8*, 041028.
- (17) Yao, W.; Li, C.; Wang, L.; Xue, S.; Dan, Y.; Iida, K.; Kamazawa, K.; Li, K.; Fang, C.; Li, Y. Topological spin excitations in a three-dimensional antiferromagnet. *Nat. Phys.* **2018**, *14*, 1011–1015.
- (18) Lee, K. H.; Chung, S. B.; Park, K.; Park, J.-G. Magnonic quantum spin Hall state in the zigzag and stripe phases of the antiferromagnetic honeycomb lattice. *Phys. Rev. B* **2018**, *97*, 180401.
- (19) Zhang, H.; Xu, C.; Carnahan, C.; Sretenovic, M.; Suri, N.; Xiao, D.; Ke, X. Anomalous thermal Hall effect in an insulating van der waals magnet. *Phys. Rev. Lett.* **2021**, *127*, 247202.
- (20) McClarty, P. A. Topological magnons: A review. *Annu. Rev. Condens. Matter Phys.* **2022**, *13*, 171–190.
- (21) Chumak, A. V.; Serga, A. A.; Hillebrands, B. Magnon transistor for all-magnon data processing. *Nat. Commun.* **2014**, *5*, 4700.
- (22) Neusser, S.; Grundler, D. Magnonics: Spin waves on the nanoscale. *Adv. Mater.* **2009**, *21*, 2927–2932.

- (23) Li, J.; Wilson, C. B.; Cheng, R.; Lohmann, M.; Kavand, M.; Yuan, W.; Aldosary, M.; Agladze, N.; Wei, P.; Sherwin, M. S.; et al. Spin current from sub-terahertz-generated antiferromagnetic magnons. *Nature* **2020**, *578*, 70–74.
- (24) Zhang, Z.; Gao, F. Y.; Curtis, J. B.; Liu, Z.-J.; Chien, Y.-C.; von Hoegen, A.; Wong, M. T.; Kurihara, T.; Suemoto, T.; Narang, P.; et al. Terahertz field-induced nonlinear coupling of two magnon modes in an antiferromagnet. *Nat. Phys.* **2024**, 1–6.
- (25) Lebrun, R.; Ross, A.; Bender, S.; Qaiumzadeh, A.; Baldrati, L.; Cramer, J.; Brataas, A.; Duine, R.; Kläui, M. Tunable long-distance spin transport in a crystalline antiferromagnetic iron oxide. *Nature* **2018**, *561*, 222–225.
- (26) Bader, S. D.; Parkin, S. S. P. Spintronics. *Annu. Rev. Condens. Matter Phys.* **2010**, *1*, 71–88.
- (27) Jungwirth, T.; Marti, X.; Wadley, P.; Wunderlich, J. Antiferromagnetic spintronics. *Nat. Nanotechnol.* **2016**, *11*, 231–241.
- (28) Liu, C.; Luo, Y.; Hong, D.; Zhang, S. S.-L.; Saglam, H.; Li, Y.; Lin, Y.; Fisher, B.; Pearson, J. E.; Jiang, J. S.; et al. Electric field control of magnon spin currents in an antiferromagnetic insulator. *Sci. Adv.* **2021**, *7*, 1669.
- (29) Parsonnet, E.; Caretta, L.; Nagarajan, V.; Zhang, H.; Taghinejad, H.; Behera, P.; Huang, X.; Kavle, P.; Fernandez, A.; Nikonov, D.; et al. Nonvolatile electric field control of thermal magnons in the absence of an applied magnetic field. *Phys. Rev. Lett.* **2022**, *129*, 087601.
- (30) Rovillain, P.; De Sousa, R.; Gallais, Y.; Sacuto, A.; Méasson, M.; Colson, D.; Forget, A.; Bibes, M.; Barthélémy, A.; Cazayous, M. Electric-field control of spin waves at room temperature in multiferroic BiFeO₃. *Nat. Mater.* **2010**, *9*, 975–979.
- (31) Rana, B.; Otani, Y. Towards magnonic devices based on voltage-controlled magnetic anisotropy. *Commun. Phys.* **2019**, *2*, 90.

- (32) Eerenstein, W.; Mathur, N.; Scott, J. F. Multiferroic and magnetoelectric materials. *Nature* **2006**, *442*, 759–765.
- (33) Fiebig, M.; Lottermoser, T.; Meier, D.; Trassin, M. The evolution of multiferroics. *Nat. Rev. Mater.* **2016**, *1*, 1–14.
- (34) Spaldin, N. A.; Cheong, S.-W.; Ramesh, R. Multiferroics: Past, present, and future. *Phys. Today* **2010**, *63*, 38–43.
- (35) Spaldin, N. A.; Ramesh, R. Advances in magnetoelectric multiferroics. *Nat. Mater.* **2019**, *18*, 203–212.
- (36) Dong, S.; Liu, J.-M.; Cheong, S.-W.; Ren, Z. Multiferroic materials and magnetoelectric physics: symmetry, entanglement, excitation, and topology. *Adv. Phys.* **2015**, *64*, 519–626.
- (37) Dong, S.; Xiang, H.; Dagotto, E. Magnetoelectricity in multiferroics: a theoretical perspective. *Natl. Sci. Rev.* **2019**, *6*, 629–641.
- (38) Neumann, R. R.; Mook, A.; Henk, J.; Mertig, I. Orbital magnetic moment of magnons. *Phys. Rev. Lett.* **2020**, *125*, 117209.
- (39) Fishman, R. S.; Gardner, J. S.; Okamoto, S. Orbital angular momentum of magnons in collinear magnets. *Phys. Rev. Lett.* **2022**, *129*, 167202.
- (40) Go, G.; An, D.; Lee, H.-W.; Kim, S. K. Magnon Orbital Nernst Effect in Honeycomb Antiferromagnets without Spin–Orbit Coupling. *Nano Lett.* **2024**, *24*, 5968–5974.
- (41) Fiebig, M. Revival of the magnetoelectric effect. *J. Phys. D* **2005**, *38*, R123.
- (42) Holstein, T.; Primakoff, H. Field dependence of the intrinsic domain magnetization of a ferromagnet. *Phys. Rev.* **1940**, *58*, 1098.
- (43) Chang, M.-C.; Niu, Q. Berry phase, hyperorbits, and the Hofstadter spectrum: Semiclassical dynamics in magnetic Bloch bands. *Phys. Rev. B* **1996**, *53*, 7010.

- (44) Xiao, D.; Chang, M.-C.; Niu, Q. Berry phase effects on electronic properties. *Rev. Mod. Phys.* **2010**, *82*, 1959–2007.
- (45) Zhang, X.; Lu, Q.; Liu, W.; Niu, W.; Sun, J.; Cook, J.; Vaninger, M.; Miceli, P. F.; Singh, D. J.; Lian, S.-W.; et al. Room-temperature intrinsic ferromagnetism in epitaxial CrTe₂ ultrathin films. *Nat. Commun.* **2021**, *12*, 2492.
- (46) Meng, L.; Zhou, Z.; Xu, M.; Yang, S.; Si, K.; Liu, L.; Wang, X.; Jiang, H.; Li, B.; Qin, P.; et al. Anomalous thickness dependence of Curie temperature in air-stable two-dimensional ferromagnetic 1T-CrTe₂ grown by chemical vapor deposition. *Nat. Commun.* **2021**, *12*, 809.
- (47) Xian, J.-J.; Wang, C.; Nie, J.-H.; Li, R.; Han, M.; Lin, J.; Zhang, W.-H.; Liu, Z.-Y.; Zhang, Z.-M.; Miao, M.-P.; et al. Spin mapping of intralayer antiferromagnetism and field-induced spin reorientation in monolayer CrTe₂. *Nat. Commun.* **2022**, *13*, 257.
- (48) Hou, Y.; Xue, F.; Qiu, L.; Wang, Z.; Wu, R. Multifunctional two-dimensional van der Waals Janus magnet Cr-based dichalcogenide halides. *npj Comput. Mater.* **2022**, *8*, 120.
- (49) Xiao, W.-Z.; Xu, L.; Xiao, G.; Wang, L.-L.; Dai, X.-Y. Two-dimensional hexagonal chromium chalcogenides with large vertical piezoelectricity, high-temperature ferromagnetism, and high magnetic anisotropy. *Phys. Chem. Chem. Phys.* **2020**, *22*, 14503–14513.
- (50) *Supporting Information includes I. Additional details of DFT calculations; II. the magnetic anisotropy of bilayer CrXY; III. the orbital Berry curvature of magnons; and IV. the magnon Hamiltonian of bilayer Cr₂Br₃Cl₃.*
- (51) Xiang, H.; Kan, E.; Wei, S.-H.; Whangbo, M.-H.; Gong, X. Predicting the spin-lattice order of frustrated systems from first principles. *Phys. Rev. B* **2011**, *84*, 224429.
- (52) Xiang, H.; Lee, C.; Koo, H.-J.; Gong, X.; Whangbo, M.-H. Magnetic properties and energy-mapping analysis. *Dalton T.* **2013**, *42*, 823–853.

- (53) Xiao, D.; Yao, W.; Niu, Q. Valley-contrasting physics in graphene: magnetic moment and topological transport. *Phys. Rev. Lett.* **2007**, *99*, 236809.
- (54) Bhowal, S.; Vignale, G. Orbital Hall effect as an alternative to valley Hall effect in gapped graphene. *Phys. Rev. B* **2021**, *103*, 195309.
- (55) Zhai, X.; Blanter, Y. M. Topological valley transport of gapped Dirac magnons in bilayer ferromagnetic insulators. *Phys. Rev. B* **2020**, *102*, 075407.
- (56) Huang, B.; Clark, G.; Navarro-Moratalla, E.; Klein, D. R.; Cheng, R.; Seyler, K. L.; Zhong, D.; Schmidgall, E.; McGuire, M. A.; Cobden, D. H.; et al. Layer-dependent ferromagnetism in a van der Waals crystal down to the monolayer limit. *Nature* **2017**, *546*, 270–273.
- (57) Xu, C.; Feng, J.; Prokhorenko, S.; Nahas, Y.; Xiang, H.; Bellaiche, L. Topological spin texture in Janus monolayers of the chromium trihalides $\text{Cr}(\text{I,X})_3$. *Phys. Rev. B* **2020**, *101*, 060404.
- (58) Bonilla, M.; Kolekar, S.; Ma, Y.; Diaz, H. C.; Kalappattil, V.; Das, R.; Eggers, T.; Gutierrez, H. R.; Phan, M.-H.; Batzill, M. Strong room-temperature ferromagnetism in VSe_2 monolayers on van der Waals substrates. *Nat. Nanotechnol.* **2018**, *13*, 289–293.
- (59) Yu, W.; Li, J.; Heng, T. S.; Wang, Z.; Zhao, X.; Chi, X.; Fu, W.; Abdelwahab, I.; Zhou, J.; Dan, J.; et al. Chemically exfoliated VSe_2 monolayers with room-temperature ferromagnetism. *Adv. Mater.* **2019**, *31*, 1903779.
- (60) Wang, X.; Li, D.; Li, Z.; Wu, C.; Che, C.-M.; Chen, G.; Cui, X. Ferromagnetism in 2D vanadium diselenide. *ACS Nano* **2021**, *15*, 16236–16241.
- (61) Eren, I.; İyikanat, F.; Sahin, H. Defect tolerant and dimension dependent ferromagnetism in MnSe_2 . *Phys. Chem. Chem. Phys.* **2019**, *21*, 16718–16725.
- (62) Zhang, Z.; Niu, J.; Yang, P.; Gong, Y.; Ji, Q.; Shi, J.; Fang, Q.; Jiang, S.; Li, H.; Zhou, X.; et al. Van der Waals epitaxial growth of 2D metallic vanadium diselenide

single crystals and their extra-high electrical conductivity. *Adv. Mater.* **2017**, *29*, 1702359.

- (63) Shen, Y.-H.; Liu, Y.; Luo, M. Electrical reversal of the magnon thermal Hall coefficient in a van der Waals bilayer antiferromagnet. *Phys. Rev. B* **2024**, *110*, 045423.
- (64) Duvjir, G.; Choi, B. K.; Jang, I.; Ulstrup, S.; Kang, S.; Thi Ly, T.; Kim, S.; Choi, Y. H.; Jozwiak, C.; Bostwick, A.; et al. Emergence of a metal-insulator transition and high-temperature charge-density waves in VSe₂ at the monolayer limit. *Nano Lett.* **2018**, *18*, 5432–5438.

For TOC only

